



Cite this: *Dalton Trans.*, 2017, **46**, 2289

## A luminescent Pt<sub>2</sub>Fe spin crossover complex†

Bernhard Schäfer,<sup>a</sup> Thomas Bauer,<sup>b</sup> Isabelle Faus,<sup>b</sup> Juliusz A. Wolny,<sup>b</sup> Fabian Dahms,<sup>b</sup> Olaf Fuhr,<sup>a,c</sup> Sergei Lebedkin,<sup>a</sup> Hans-Christian Wille,<sup>d</sup> Kai Schlage,<sup>d</sup> Katharina Chevalier,<sup>b</sup> Fabian Rupp,<sup>b</sup> Rolf Diller,<sup>b</sup> Volker Schünemann,<sup>b</sup> Manfred M. Kappes<sup>a,e</sup> and Mario Ruben<sup>\*a,f</sup>

A heterotrinnuclear [Pt<sub>2</sub>Fe] spin crossover (SCO) complex was developed and synthesized employing a ditopic bridging bpp-alkynyl ligand **L** and alkynyl coordinated Pt<sup>II</sup> terpy units: [Fe<sup>II</sup>(L-Pt<sup>II</sup>)<sub>2</sub>(BF<sub>4</sub>)<sub>2</sub>] (**1**). We identified two different types of crystals of **1** which differ in their molecular packing and the number of co-crystallized solvent molecules: **1**<sup>H</sup> (1.3.5CH<sub>2</sub>Cl<sub>2</sub> in P1) and **1**<sup>L</sup> (1.10CH<sub>2</sub>Cl<sub>2</sub> in C2/c); while **1**<sup>L</sup> shows a reversible SCO with a transition temperature of 268 K, the analogous compound **1**<sup>H</sup> does not show any SCO and remains blocked in the HS state. The temperature-dependent magnetic properties of **1**<sup>H</sup> and **1**<sup>L</sup> were complementarily studied by Mössbauer spectroscopy. It has been shown that **1**<sup>L</sup> performs thermal spin crossover and that **1**<sup>L</sup> can be excited to a LIESST state. The vibrational properties of **1** were investigated by experimental nuclear resonance vibrational spectroscopy. The experimentally determined partial density of vibrational states (pDOS) was compared to a DFT-based simulation of the pDOS. The vibrational modes of the different components were assigned and visualized. In addition, the photo-physical properties of **1** and L-Pt were investigated in the solid state and in solution. The ultrafast transient absorption spectroscopy of **1** in solution was carried out to study the PL quenching channel *via* energy transfer from photoexcited Pt<sup>II</sup> terpy units to the Fe<sup>II</sup>-moiety.

Received 16th November 2016,  
Accepted 12th January 2017

DOI: 10.1039/c6dt04360g

rsc.li/dalton

## 1. Introduction

Ditopic bridging ligands are of continuing interest to covalently integrate different metal ions into molecular metal complexes.<sup>1</sup> The synthesis of homo- and hetero-multi-metal complexes such as metal-complexes containing supramolecular and macromolecular species, *e.g.* polymers, dendrimers, molecular wires and further oligonuclear metal complexes, is

based on such ligands with at least two metal binding domains.<sup>2–5</sup> If the coordination sites of ditopic ligands differ in the metal chelating properties, discrimination by means of optimized synthetic protocols yields easily dinuclear complexes of two different metal ions. The resulting complexes combine different catalytic, magnetic, and photo-physical properties and may enable a new cooperative functionality.<sup>6–9</sup> Perhaps the most adaptable and established ligands for this purpose are 2,2':6',2''-terpyridine (terpy) derivatives. They can be easily prepared using established protocols to substitute diverse positions at the central and the two peripheral pyridine rings. Substitution at the *para* position of the terpy backbone is especially developed, and facilitates [M(terpy)<sub>2</sub>]<sup>2+</sup> units to be integrated into numerous types of chemical structures.<sup>10–12</sup> A similar heterocyclic ligand with a tridentate nitrogen (N<sub>3</sub>) donor set is 2,6-bis(pyrazolyl-1-yl)pyridine (bpp), which can also be substituted at various ring positions of the central pyridine and the peripheral pyrazole rings.<sup>13–15</sup> Even though bpp-systems have been less often studied as compared to terpy-systems, two classes of bpp complexes have attracted particular attention. The first class are lanthanoid complexes of bpp-containing podants which efficiently emit light in solution.<sup>16–20</sup> The second class are Fe<sup>II</sup> complexes of bispyrazolylpyridines which often undergo thermal spin crossover (SCO) close to ambient temperature.<sup>14,21–23</sup>

<sup>a</sup>Institut für Nanotechnologie, Karlsruher Institut für Technologie (KIT), Campus Nord, Hermann-von-Helmholtz-Platz 1, 76344 Eggenstein-Leopoldshafen, Germany. E-mail: Mario.Ruben@kit.edu

<sup>b</sup>Fachbereich Physik, Technische Universität Kaiserslautern, Erwin-Schrödinger-Str. 46, 67663 Kaiserslautern, Germany

<sup>c</sup>Karlsruhe Nano-Micro Facility (KNMF), Karlsruher Institut für Technologie (KIT), Campus Nord, Hermann-von-Helmholtz-Platz 1, 76344 Eggenstein-Leopoldshafen, Germany

<sup>d</sup>Deutsches Elektronen-Synchrotron, Notkestr. 85, D-22607 Hamburg, Germany

<sup>e</sup>Institut für Physikalische Chemie, Karlsruher Institut für Technologie (KIT), Fritz-Haber-Weg 2, 76131 Karlsruhe, Germany

<sup>f</sup>Institut de Physique et Chimie des Matériaux de Strasbourg (IPCMS), CNRS-Université de Strasbourg, 23, rue du Loess, BP 43, 67034 Strasbourg cedex 2, France

† Electronic supplementary information (ESI) available. CCDC 1510868–1510870. For ESI and crystallographic data in CIF or other electronic format see DOI: 10.1039/c6dt04360g

The change in the spin state can steer the physical and chemical properties and can be monitored by a wide variety of methods, for example, IR, Mössbauer, NMR, Raman, UV/vis, and X-ray absorption spectroscopies (XAS), conductometry, dielectrometry, diffractometry, refractometry, and magnetometry.<sup>24–31</sup> The colour of the Fe<sup>II</sup>-bpp complexes changes from pale yellow in the HS state to red in the LS state.<sup>32–34</sup> To develop and investigate complexes with these application-relevant properties further, several groups have prepared bpp derivatives substituted at the 4-position of the pyridine, yielding luminescent or SCO compounds with a wide range of different and complementary functionalities.<sup>19,23,32–57</sup> Notably, only a few back-to-back ligand motifs have been developed up to now, containing two 1-bpp residues interlinked by (a) 1,2-ethenediyl,<sup>36</sup> (b) 1,4-phenylenediyl,<sup>46,50</sup> (c) 1,4-diphenylenediyl,<sup>58</sup> and (d) disulfide spacers.<sup>37,59</sup> The coordination reaction of the first three ligands with Fe<sup>II</sup> ions yields 1D coordination polymers containing covalently linked [Fe(bpp)<sub>2</sub>]<sup>2+</sup> units. The 1,4-phenylene-linked Fe<sup>II</sup> oligomer undergoes a cooperative spin transition just above room temperature.<sup>46</sup> Chandrasekar *et al.* introduced alkyl chains into the bpp chelates to enhance the solubility of the ligands and the resulting coordination polymers of Zn<sup>II</sup> and Fe<sup>II</sup>.<sup>60,61</sup> In contrast to the aforementioned polymeric behaviour, the disulfide ligand yields soluble oligomeric complexes of a tetrameric structure.<sup>59</sup> To our knowledge, only one back-to-back ligand with different metal binding domains, a dipyrazolypyridine (bpp) and a dipicolylamine (dpa), has been reported so far.<sup>62</sup> The resulting heterotrimeric FePd<sub>2</sub> and FePt<sub>2</sub> complexes are straightforward in their preparation since the two platinum metals exclusively prefer the coordination to the dpa moiety.

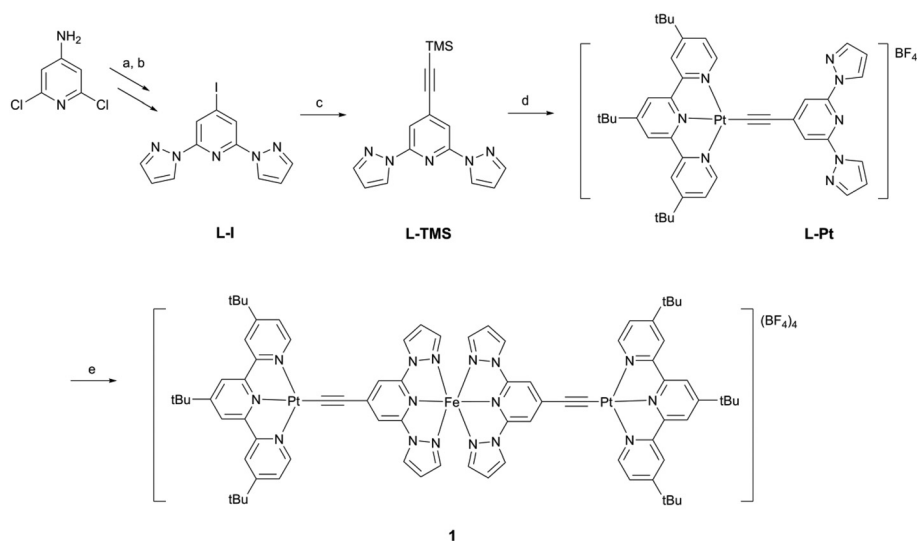
Here we report on a heteroditopic bpp-alkynyl ligand and the resulting heterotrimeric organometallic complex containing one Fe<sup>II</sup> ion in an N<sub>6</sub> bpp environment and two terminally

alkynyl coordinated Pt<sup>II</sup> terpy units. The latter are well known to show bright luminescence<sup>63–70</sup> and they form intermolecular interactions, for example, metal...metal and/or ligand...ligand ( $\pi\cdots\pi$ ) interactions. These interactions might play an important role concerning the SCO properties since supramolecular approaches (coordination polymers, hydrogen bonding,  $\pi\cdots\pi$  stacking, *etc.*) have been applied to molecular spin transition (ST) units, partially with the objective to increase the magnitude of cooperativity and ST temperatures.<sup>71–74</sup> There are only very few examples of luminescent SCO complexes in the literature.<sup>75</sup> A terminal ethynyl group was chosen since it is known to form relatively strong platinum  $\sigma$ -alkynyl bonds. In comparison with previously reported homoditopic 1-bpp<sup>36,46,50</sup> and bis-alkynyl<sup>76,77</sup> ligands, the heteroditopic bpp-alkynyl ligand described here provides a new perspective of the efficient preparation of organometallic complexes with two different metals.

## 2. Experimental results

### 2.1. Synthesis and structure

The employed ligand, 2,6-di(pyrazol-1-yl)-4-(trimethylsilylethynyl)pyridine (Scheme 1), was prepared from commercial 2,6-dichloro-4-amino pyridine in three synthetic steps.<sup>48,78</sup> The Pt acetylide **L-Pt** was formed following the synthetic procedure reported by Hagihara *et al.*<sup>79</sup> employing a bpp-acetylide, which was formed in an *in situ* protodesilylation reaction of the trimethylsilyl (TMS) protected TMS-ethynyl precursor **L-TMS** with K<sub>2</sub>CO<sub>3</sub>. The reaction between the platinum chloride precursor (tbtpyPtCl)(BF<sub>4</sub>) (tbtpy: 4,4',4''-tri-*tert*-butyl-2,2':6',2''-terpyridine) and the acetylide is facilitated under basic conditions using triethylamine, which deprotonates the acetylide ligand, while the Cu<sup>+</sup> ion activates the coupling reac-



**Scheme 1** Synthesis of ligands and complexes. Reaction conditions: (a) pyrazole, K, diglyme, 110 °C; (b) KI<sub>2</sub>, I, CH<sub>2</sub>Cl<sub>2</sub>/iso-amyl nitrite, 75 °C; (c) TMSA (trimethylsilylacetylene), Pd(PPh<sub>3</sub>)<sub>4</sub>, CuI, N(CH<sub>2</sub>CH<sub>3</sub>)<sub>3</sub>, THF, 25 °C; (d) [(tbtpy)PtCl](BF<sub>4</sub>), K<sub>2</sub>CO<sub>3</sub>, THF/CH<sub>3</sub>OH/N(Et)<sub>3</sub>/H<sub>2</sub>O, CuI, 25 °C; (e) Fe(H<sub>2</sub>O)<sub>6</sub>(BF<sub>4</sub>)<sub>2</sub>, CH<sub>3</sub>CN, 50 °C.

tion by coordination to the acetylide bond forming a cuprate. In a final *trans*-metallation reaction the Pt–acetylide bond is formed. In order to prevent the oxidation of the Cu catalyst, the reaction is conducted under a deoxygenated atmosphere. After work-up and column chromatography, it was possible to obtain **L-Pt** in a good yield of 70% as a bright yellow powder.

1D and 2D NMR spectroscopy was used to characterize the compound **L-Pt** completely. The ESI TOF mass spectrometry of the compound showed the monocation of  $[(\mathbf{L-Pt})\text{-BF}_4]$  without the counter ion, Fig. S1.† Single crystals suitable for X-ray diffraction were obtained from the  $\text{PF}_6$  salt of **L-Pt**. The molecular structure of **L-Pt** is shown in Fig. 1a. One unit cell contains two complex molecules of **L-Pt** co-crystallizing with two molecules of acetonitrile (top view in Fig. 1b). The arrangement in a head-to-tail configuration causes a rather long Pt–Pt distance of 6.5 Å. The (tbtpy)Pt unit is in one plane with the coordinated bpp-acetylide, side view in Fig. 1c.

Treatment of a yellow acetonitrile solution of **L-Pt** with a half equivalent of  $[\text{Fe}^{\text{II}}(\text{H}_2\text{O})_6](\text{BF}_4)_2$  afforded an orange solution of the heterotrimeric complex **1**. The solvent was removed. Elemental analysis,  $^1\text{H}$  NMR and IR spectroscopy supported the formation of the product as the desired  $[\text{Fe}^{\text{II}}(\mathbf{L-Pt})_2](\text{BF}_4)_2$  (**1**, Scheme 1). An acetonitrile solution of **1** was subjected to ESI-TOF mass spectrometry. The spectrum showed two signals, a strong one corresponding to  $[(\mathbf{L-Pt})\text{-BF}_4]^+$  and a weak signal corresponding to the  $[\mathbf{1-2BF}_4]^{2+}$  cation with the mass to charge ratio of  $m/z = 945.301$  (simulated 945.297), showing a perfectly matching isotope pattern compared to a simulated spectrum (Fig. S3†).

Upon  $\text{Fe}^{\text{II}}$  coordination the  $^1\text{H}$  NMR spectrum of **1** in  $\text{CD}_3\text{CN}$  showed that the four 1-bpp-based signals have been shifted paramagnetically to lower fields (40–70 ppm), Fig. S5.† The tbtpy-based resonances remained in the expected region <9 ppm, Fig. S4.† In solution, complex **1** has  $C_2$  symmetry due to identical chemical shifts of both **L-Pt** subunits. A colour change of the NMR sample after a few days of being kept in  $\text{CD}_3\text{CN}$  revealed the de-complexation of  $\text{Fe}^{\text{II}}$  leading to free **L-Pt** in the sample. Solution tests in methanol showed instantaneous dissociation to free **L-Pt** and solvated  $\text{Fe}^{\text{II}}$  species. Due to the six *tert*-butyl groups of tbtpy present in **1**, it is possible to dissolve this tetra-cationic complex in dichloromethane, which is a non-coordinating solvent of low polarity. Fortunately, the complex was long-term stable in dichloromethane and single crystals suitable for X-ray analysis were

obtained by slow evaporation. We found two types of crystals of **1** growing in a dichloromethane solution. They were slightly different in colour, one sample having reddish orange and the other yellowish orange appearance. Nevertheless, it was possible to solve the molecular structure of both types of crystals by single crystal X-ray diffraction.

Indeed, we found in both samples the expected complex **1** (Scheme 1) containing an  $\text{Fe}^{\text{II}}$  and two  $\text{Pt}^{\text{II}}$  ions. The difference between the structures was the amount of solvent molecules incorporated into the crystal lattice (resulting in different packings in different space groups,  $P\bar{1}$  and  $C2/c$ , respectively), in our case dichloromethane, and surprisingly the spin state of the  $\text{Fe}^{\text{II}}$  ion.

The moiety formula of the first species (yellowish orange coloured), which is  $[\text{Fe}(\mathbf{L-Pt})_2](\text{BF}_4)_2 \cdot 3.5\text{CH}_2\text{Cl}_2$ , contains three and half molecules of  $\text{CH}_2\text{Cl}_2$  per complex **1** with the  $\text{Fe}^{\text{II}}$  ion in the high spin (HS) state, hereafter called **1<sup>H</sup>**. The moiety formula of the second species (reddish orange coloured) is  $[\text{Fe}(\mathbf{L-Pt})_2](\text{BF}_4)_2 \cdot 10\text{CH}_2\text{Cl}_2$  with the  $\text{Fe}^{\text{II}}$  ion in the low spin (LS) state, hereafter called **1<sup>L</sup>**. At 180 K, **1<sup>L</sup>** has Fe–N bond lengths with typical values for the LS state (average bond lengths  $d$  [pm]: Fe–N 194, see Table 1). Other indicators of the spin state in related  $\text{Fe}^{\text{II}}$ -bis(pyrazol-1-yl)pyridine complexes are the  $N_{\text{pyrazole}}\text{-Fe-N}_{\text{pyrazole}}$  angles (*ca.* 160° for LS and 145° for HS) and the  $\Sigma$  parameter (*ca.* 90° for LS and 160° for HS).<sup>55,80,81</sup> According to the determined  $N_{\text{pyrazole}}\text{-Fe-N}_{\text{pyrazole}}$  angles of  $N(1)\text{-Fe}(1)\text{-N}(5)$  160.5(2)° and  $N(1)'\text{-Fe}(1)\text{-N}(5)'$  160.5(2)°, and the calculated  $\Sigma = 94$ , one can conclude that the  $\text{Fe}^{\text{II}}$  ion in **1<sup>L</sup>** is in the LS state. The same parameters for **1<sup>H</sup>** (average bond lengths  $d$  [pm]: Fe–N 216,  $N(1)\text{-Fe}(1)\text{-N}(5)$  146° and  $N(6)\text{-Fe}(1)\text{-N}(10)$  140°, and a  $\Sigma$  value of 169) indicate that the  $\text{Fe}^{\text{II}}$  ion is in the HS state, Table 1. A number of further distortion parameters for the local coordination geometry about the iron centre of **1<sup>H</sup>** and **1<sup>L</sup>** were determined and are tabulated in the ESI (Table S3†).

The coordinated Pt(II) metal ions adopt an essentially square-planar but slightly distorted geometry due to the coordination constraints imposed by the ligand backbone of the terpy ligand.

In both crystal structures, we found a linear chain-like arrangement of the heterotrimeric complexes formed by intermolecular stacking of Pt-terpy moieties of two neighbouring complexes in a head-to-tail configuration exhibiting weak  $\text{Pt}(\text{II})\cdots\text{Pt}(\text{II})$  interactions with an average distance of about 3.3 Å, Fig. 2. **1<sup>L</sup>** crystallizes in a monoclinic crystal system and

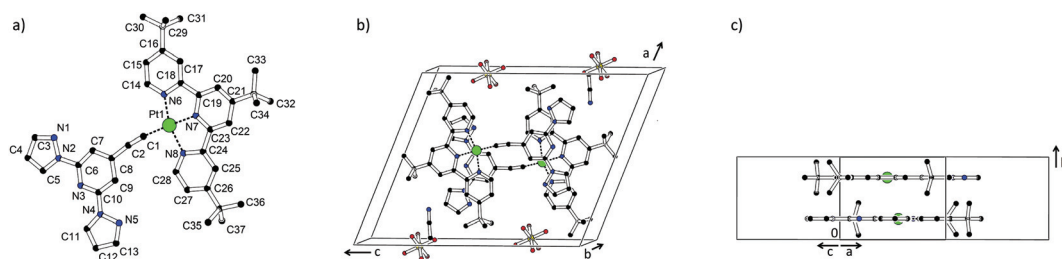


Fig. 1 View of the molecular structure of the **L-Pt**; H atoms are not shown, and solvent molecules and anions are omitted for clarity in (a) and (c).

**Table 1** Bond lengths (pm), significant angles (°) and the naming scheme adopted for the iron coordination sphere in **1<sup>L</sup>** and **1<sup>H</sup>**

Compound	<b>1<sup>L</sup></b>	<b>1<sup>H</sup></b>	
<i>T</i> (K)	180	180	
Bond length (pm)	Fe(1)–N(3)	188.5(5)	212.2(6)
	Fe(1)–N(3)′	188.5(5)	214.8(7)
	Fe(1)–N(1)′	196.3(6)	216.5(8)
	Fe(1)–N(1)	196.3(6)	216.7(8)
	Fe(1)–N(5)′	197.2(6)	217.9(8)
	Fe(1)–N(5)	197.2(6)	220.4(8)
	Fe(1)–N(10)		220.4(8)
Angles (°)	N(1)–Fe(1)–N(5)	160.6(2)	145.6(3)
	N(1)′–Fe(1)–N(5)′	160.6(2)	140.3(3)
$\Sigma\text{Fe}1^a$	94	169	
Colour	Reddish-orange	Yellowish orange	
Spin status	LS	HS	

$$^a \Sigma = \sum_{i=1}^{12} |\phi_i - 90|, \text{ where } \phi_i \text{ is an N–Fe–N octahedron angle with two N atoms in } cis.$$

the space group *C2/c* with half a molecule per asymmetric unit (with the *C*<sub>2</sub> axis through the Fe atom). Therefore, only one type of stacking with a Pt1–Pt1 distance of 3.326 Å is present. The situation in **1<sup>H</sup>** is different since it is possible to distinguish the two Pt-terpy moieties of the complex in the solid state due to the triclinic space group *P1̄*: with one molecule in the asymmetric unit. The chain-like arrangement in **1<sup>H</sup>** shows an alternation between two Pt1 and two Pt2 units with a Pt1–Pt1 distance of 3.259 Å and a Pt2–Pt2 distance of 3.303 Å (Fig. 2). These Pt(*n*)⋯Pt(*n*) distances are within the normal range for related Pt(*n*)-terpy complexes.<sup>82</sup>

Unfortunately, it was not possible to completely separate the different crystals from each other to investigate samples with just one type of crystal present. It was also noticed that the crystals rapidly aged after being removed from the CH<sub>2</sub>Cl<sub>2</sub> atmosphere. The reason for this behaviour is apparently the loss of the co-crystallizing CH<sub>2</sub>Cl<sub>2</sub> molecules. The crystals lost their apparent shape during this process and formed a powdery sample.

## 2.2. Magnetic properties

To quantify the magnetism of complex **1**, temperature-dependent magnetometry was carried out (Fig. 3). A  $\chi T$  value

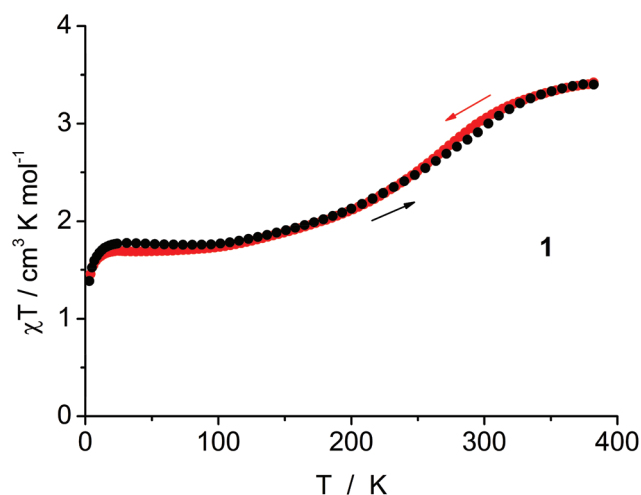


**Fig. 3** Magnetic properties of compound **1**; the  $\chi T$  plot (*B* = 0.1 T) shows the presence of two different species, one with SCO properties (**1<sup>L</sup>**) and another one trapped in the HS state (**1<sup>H</sup>**).

of 3.4 cm<sup>3</sup> K mol<sup>−1</sup> was observed at a temperature of 380 K but a gradual decrease exhibiting an inflection point at 268 K sets in on decreasing the temperature, typical features of a SCO

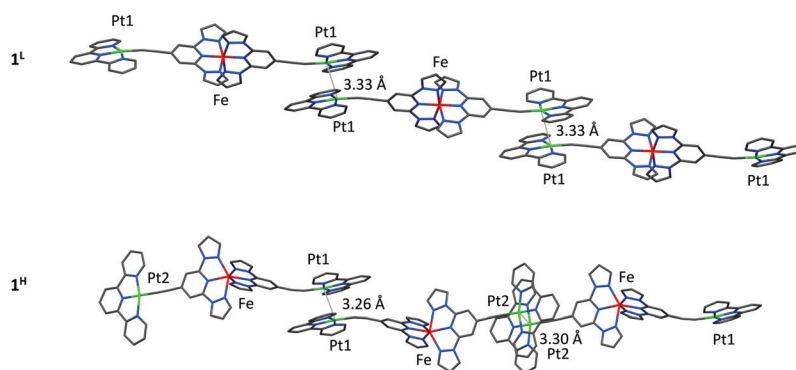


**Fig. 2** Representation of the linear chain-like arrangement of **1<sup>H</sup>** and **1<sup>L</sup>** formed by intermolecular stacking of two Pt-terpy moieties of two neighbouring complexes in a head-to-tail configuration and the Pt–Pt distance (butyl groups and H atoms are omitted for clarity; Pt: green, Fe: red, N: blue, C: grey).

behaviour converting Fe<sup>II</sup> from high-spin (HS,  $S = 2$ ) into low-spin (LS,  $S = 0$ ) states. At temperatures below 85 K the  $\chi T$  value reaches a plateau of  $1.7 \text{ cm}^3 \text{ K mol}^{-1}$ , a value which indicates that 50% of the Fe<sup>II</sup> ions changed their spin state from HS to LS. Only below 20 K the  $\chi T$  value does decrease again reaching a minimum value of  $1.3 \text{ cm}^3 \text{ mol K}^{-1}$  at 2 K. This drop is attributed to the zero-field splitting of the energy levels of the Fe<sup>II</sup> HS ions in an octahedral coordination environment. The other 50% of Fe<sup>II</sup> ions remain in the HS state; this situation can be explained by the X-ray structure of **1**<sup>H</sup> which shows a distorted Fe<sup>II</sup> ion trapped in the HS state. Such a behaviour was found before in strongly distorted octahedral Fe-bpp complexes, e.g. of pyrene-substituted 2,6-bpp or in  $[2 \times 2]\text{Fe}^{\text{II}}$  grid complexes.<sup>54,83</sup>

A <sup>57</sup>Fe enriched sample of complex **1** was investigated using Mössbauer spectroscopy with externally applied magnetic fields of up to  $B = 5 \text{ T}$ . The analysis of the Mössbauer data obtained at  $B = 30 \text{ mT}$  (Fig. 4a) shows the presence of the two components **1**<sup>L</sup> and **1**<sup>H</sup> with a relative ratio of 1 : 1. The field-dependent Mössbauer spectra displayed in Fig. 4b–e have been analysed by the spin-Hamiltonian formalism.<sup>84–86</sup> The first component has been simulated with  $S = 0$ , an isomer shift of  $\delta = 0.40 \text{ mm s}^{-1}$  and a quadrupole splitting of  $\Delta E_Q = 0.75 \text{ mm s}^{-1}$ . Thus, this component can be assigned to the low-spin species

**1**<sup>L</sup>.<sup>84,85</sup> The second component shows  $\delta = 1.11 \text{ mm s}^{-1}$  and  $\Delta E_Q = 3.43 \text{ mm s}^{-1}$ . These parameters are characteristic of Fe<sup>II</sup> HS ( $S = 2$ )<sup>84,85</sup> as confirmed by the spin-Hamiltonian simulations. This leads to the conclusion that the second component originates from **1**<sup>H</sup>. The thus obtained zero-field splitting parameter  $D$ , the rhombicity  $E/D$ , and the hyperfine coupling tensor elements  $A_{xx}/\mu_{\text{N}}g_{\text{N}}$ ,  $A_{yy}/\mu_{\text{N}}g_{\text{N}}$  and  $A_{zz}/\mu_{\text{N}}g_{\text{N}}$  are also listed in Table 2. The values of the  $A$ -tensor elements are quite small compared to e.g. isolated Fe<sup>II</sup> HS centres in proteins, which are in the range of  $-18$  to  $-20 \text{ T}$ .<sup>86,87</sup> The reason for this observation is as yet unclear. It may be explained by a field induced antiferromagnetic ordering phenomenon at  $T = 5 \text{ K}$  or by the presence of intermolecular spin-spin relaxation with relaxation times compared to the characteristic time window of <sup>57</sup>Fe Mössbauer spectroscopy ( $\sim 10^{-7} \text{ s}$ ) even at high fields of  $5 \text{ T}$ .<sup>87</sup>

The transition from LS to HS in a SCO compound can also be induced by light irradiation (Light-Induced Excited Spin-State Trapping (LIESST)) at temperatures below typically  $50 \text{ K}$ .<sup>22</sup> Fig. 5 shows a Mössbauer spectrum of **1** taken at  $T = 4.2 \text{ K}$  before (Fig. 5a) and immediately after irradiating the same sample with red laser light ( $\lambda = 635 \text{ nm}$ ) for about 17 hours (Fig. 5b). There is a transition of 88% of component **1**<sup>L</sup> to a LIESST state which is represented by component **1**<sup>H</sup>

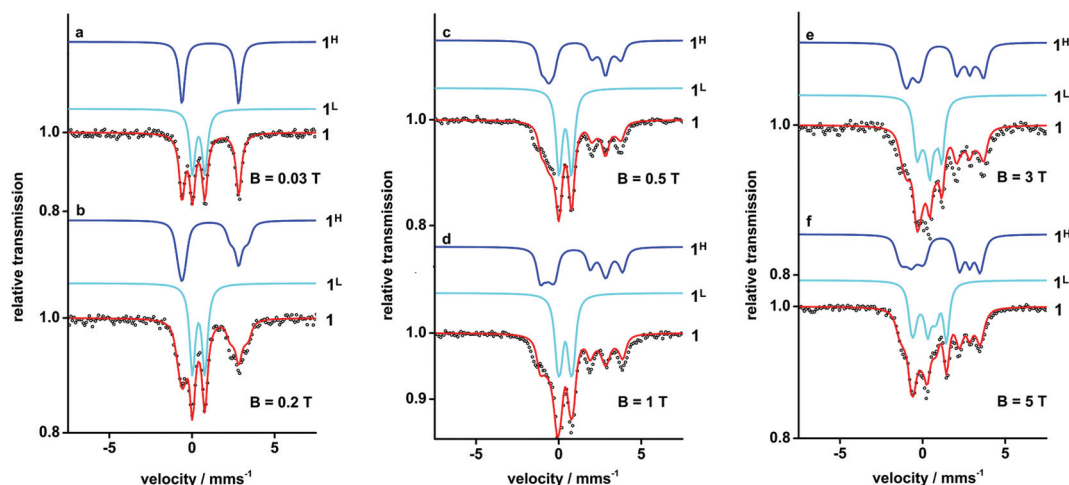


**Fig. 4** (a) Mössbauer spectrum of **1** obtained at  $T = 5 \text{ K}$  and  $B = 30 \text{ mT}$ . The red solid line represents the sum of two Lorentzian doublets; (b) to (g) field-dependent Mössbauer spectra obtained at  $T = 5 \text{ K}$  and the indicated external fields. The simulations (red solid lines) have been obtained by a spin-Hamiltonian analysis<sup>84–86</sup> employing simultaneous fitting of all displayed data sets. For parameters see Table 2 and the text; each simulated spectrum consists of two components (blue and cyan), with a relative area of 1 : 1, shown separately with coloured lines; all spectra were taken with fields applied parallel to the  $\gamma$ -beam.

**Table 2** Mössbauer parameters of **1** as obtained from the spin-Hamiltonian simulations shown in Fig. 4

Component	Spin	$\delta$ [ $\text{mm s}^{-1}$ ]	$\Delta E_Q$ [ $\text{mm s}^{-1}$ ]	$\eta$	$\Gamma$ [ $\text{mm s}^{-1}$ ]	$D$ [ $\text{cm}^{-1}$ ]	$E/D$	$g_{xx,yy,zz}$	$A_{xx,yy,zz}/\mu_{\text{N}}g_{\text{N}}$ [T]	Relative area [%]
<b>1</b> <sup>L</sup>	$S = 0$	0.40	-0.75	0.0	0.40	—	—	—	—	50
<b>1</b> <sup>H</sup>	$S = 2$	1.11	-3.43 <sup>a</sup>	0.0	0.40	2.1	0.23	2.0	-2.0, -4.9, -0.2	50

<sup>a</sup> Determined by Mössbauer spectroscopic measurements at  $T = 150$  and  $T = 200 \text{ K}$  with an applied external magnetic field of  $B = 5 \text{ T}$ , shown in the ESI S6a.

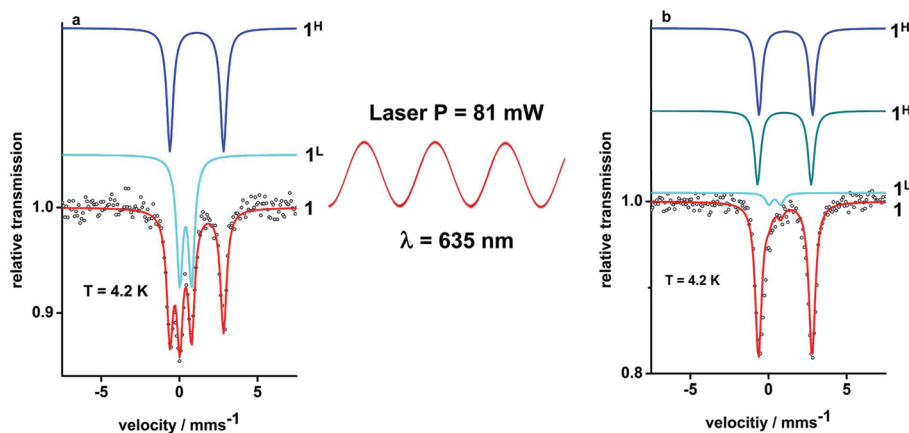


Fig. 5 Mössbauer spectra of **1** obtained at  $T = 4.2$  K (a) before and (b) after irradiating with red laser light ( $\lambda = 635$  nm; input power  $P = 81$  mW; irradiation time  $t \approx 17$  h). Comparison of (a) and (b) indicates a significant decrease of the LS component  $1^L$  and the rise of a new component,  $1^{H'}$ , with a relative percentage share of 43%. The line width is  $\Gamma = 0.48$  mm s $^{-1}$  for all three species.

with  $\delta = 1.03$  mm s $^{-1}$  and  $\Delta E_Q = 3.43$  mm s $^{-1}$ . It should be noted that irradiation does not change the amount of component  $1^H$  in the sample.

In conclusion, it has been shown by Mössbauer spectroscopy that  $1^L$  performs thermal spin crossover and that  $1^L$  can be excited to a LIESST state by irradiation with red light. On the contrary,  $1^H$  with a relative share of 50% has no SCO abilities and is trapped in the HS state over the full temperature range (from 4.2 K to 280 K). This is in perfect agreement with the results obtained from magnetometry (Fig. 3).

In order to obtain insight into the vibrational properties of the HS and LS forms of **1**, nuclear resonance vibrational spectroscopy (NRVS) was performed. This technique is based on the Mössbauer effect and is able to detect selectively iron ligand vibrations in molecular systems.<sup>88,89</sup> Since the  $^{57}\text{Fe}$  nucleus serves as a nuclear probe, NRVS is especially suitable

for detecting iron ligand modes in iron containing SCO complexes.<sup>90</sup>

Fig. 6a and b show the partial density of vibrational states (pDOS) determined from the NRVS data of **1** obtained at 80 and 300 K. The pDOS obtained at 80 K (Fig. 6a) shows two broad bands centered at about 220 and 275 cm $^{-1}$ . This spectral region is characteristic of spin marker bands corresponding to iron ligand vibrations of the HS state. Fig. 6c shows a DFT-based simulation of the pDOS under the assumption that 50% of the molecules are in the HS state and have the structure  $1^H$  whereas the other 50% are in the LS state having the structure  $1^L$  as indicated by the magnetometry (Fig. 3) and the Mössbauer data (Fig. 4). The simulation displays a broad band structure in the region between 200 and 300 cm $^{-1}$ . A characteristic band at 213.2 cm $^{-1}$  is due to a molecular mode which involves HS iron movement in a direction which is applied per-

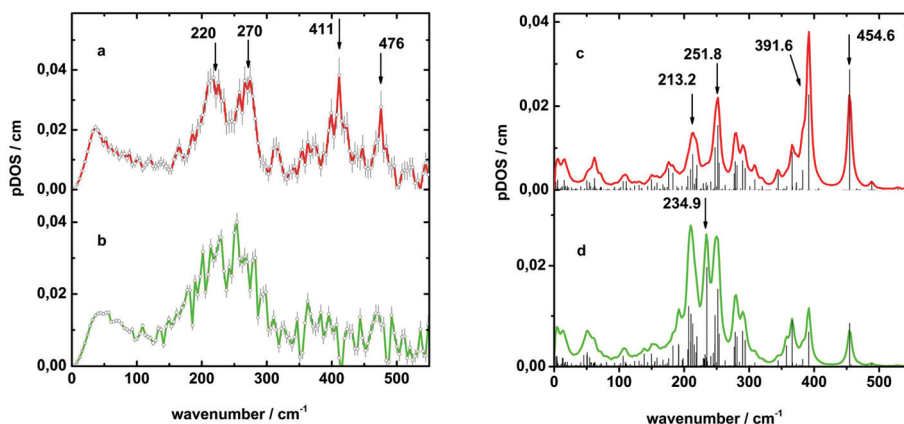


Fig. 6 Experimentally determined pDOS of **1** obtained at (a)  $T = 80$  K and (b)  $T = 300$  K. (c) DFT-based simulation of the pDOS assuming a HS to LS fraction of **1** : **1** using Gaussian09 Rev. D.01 (B3LYP/CEP31 G, see ESI†). The HS and LS fractions have been calculated based on the structure of  $1^H$  and  $1^L$ , respectively; (d) simulated pDOS representing the sum of three components: 50% HS ( $1^H$ ), 15% LS ( $1^L$ ) and 35% HS ( $1^{H'}$ ) molecules which have switched from LS to HS by retaining the straight molecular structure of  $1^L$ . The vertical lines highlight the quadratic displacement of the iron atoms as a function of the energy of the corresponding vibrations.

pendicular to the long Pt–Pt axis of the  $1^H$  structure (see Table S2 and movie FePt\_trapped\_HS213†). The molecular mode calculated to occur at  $251.8\text{ cm}^{-1}$  has an iron motion with projections both along the long Pt–Pt axis and perpendicular to it (movie FePt\_trapped\_HS251†). For a detailed list of the calculated modes see Table S2 and the corresponding movies given in the ESI.†

In the region between  $300$  and  $500\text{ cm}^{-1}$ , the experimental pDOS obtained at  $80\text{ K}$  shows two prominent relatively sharp bands at  $411\text{ cm}^{-1}$  and  $476\text{ cm}^{-1}$  (Fig. 6a). This spectral region is typical for spin marker bands of the  $\text{Fe}^{II}$  LS state. Thus, the two vibrational bands at  $411$  and  $476\text{ cm}^{-1}$  originate from the LS  $\text{Fe}^{II}$  ion in  $1^L$  as is also indicated by the displayed simulation in Fig. 6c. The intense band at  $392\text{ cm}^{-1}$  in the simulated pDOS consists of bands from 4 molecular modes involving LS iron motion: two degenerate modes at  $382.4\text{ cm}^{-1}$  and two degenerate ones at  $391.6\text{ cm}^{-1}$ . These molecular modes are very similar to each other and in all four modes the iron moves perpendicular to the Pt–Pt axis (watch movies FePt\_LS\_382a, FePt\_LS\_382b, FePt\_LS\_391a, FePt\_LS\_391b†). The experimental band occurring at  $476\text{ cm}^{-1}$  (Fig. 6c) can be assigned to a single molecular mode calculated to be at  $454.6\text{ cm}^{-1}$  in which the iron is moving along the Pt–Pt-axis (movie FePt\_LS\_454†). The experimental pDOS obtained at  $300\text{ K}$  (Fig. 6b) shows significant spectral features from  $150$  up to  $320\text{ cm}^{-1}$ . The most distinct bands have their maxima at  $202$ ,  $214$ ,  $230$ ,  $254$ ,  $282$ , and  $294\text{ cm}^{-1}$ . Fig. 6d shows the corresponding simulation which has been performed with 3 components: (i) a first component was calculated assuming the iron being in the HS state based on the structure  $1^H$  (50%), (ii) a second one with the iron being in the LS state (15%; structure  $1^L$ ), and (iii) a third component, hereafter called  $1^H$ , originates from  $1^L$  which has undergone SCO to the HS state at  $300\text{ K}$ . For the DFT calculation of  $1^H$  a structural model has been created by switching the iron spin state from LS to HS and retaining the straight molecular structure of  $1^L$  (for details see ESI†). The structure of the almost linear  $1^H$  differs from the more bent structure of  $1^H$ ; therefore it is not surprising that the calculated HS iron ligand modes are slightly different from each other (Fig. S8a/b†). A strong band evolves at  $234.9\text{ cm}^{-1}$  during the SCO of  $1^L$  to  $1^H$ . This band is caused by a molecular mode of the central HS iron moving along the Pt–Pt-axis (Fig. S8b and movie FePt\_HS\_234†). At  $300\text{ K}$ , two residual computed LS marker bands are still visible at higher wavenumbers (calculated to occur at  $392$  and  $454.6\text{ cm}^{-1}$ , Fig. 6d). The experimental LS marker modes (at  $411$  and  $476\text{ cm}^{-1}$ , Fig. 6b) are not distinct due to the LS contribution of only 15% in total at this temperature.

### 2.3. Photophysical properties

The photophysical properties of  $1$  were investigated in solution (UV-vis absorption spectroscopy, transient absorption spectroscopy, and PL spectroscopy) and in the solid state (UV-vis absorption spectroscopy and PL spectroscopy). It has to be considered that all magnetic measurements were carried out with solid samples. The time resolved femtosecond-transient

absorption spectroscopy provides detailed information concerning the photophysical processes taking place after excitation with light. At first, we will discuss the investigations in the solid state and later in solution.

### 2.4. Photoluminescence

In the absorption spectra of optically ‘thick’ solid samples of  $1$  and **L-Pt** (measured using an integrating sphere), the onset of absorption is observed at  $\sim 600$  and  $520\text{ nm}$ , respectively, whereas the bands at shorter wavelengths appear to be saturated (Fig. 7d).

PL spectra of solid  $1$  and **L-Pt** are also quite similar (Fig. 7). The moderately intense emission is apparently contributed by two components: a vibronically-structured band within  $\sim 500$ – $600\text{ nm}$ , which corresponds to  $\sim 520\text{ nm}$  emission of  $1$  and **L-Pt** in solution (Fig. 8b), and a broad feature at  $\sim 650\text{ nm}$ . The relative intensity of the first band diminishes at elevated temperatures, so that the PL is dominated by the second band at ambient temperature. The PL lifetimes (extracted from bi-exponential fits) lie on the time scale of microseconds at low temperatures and are notably longer for the band at  $\sim 650\text{ nm}$ . The PL decays faster upon increasing the temperature, roughly correlating with the decrease in intensity. The first and second components of the solid-state emission of  $1$  and **L-Pt** may be attributed to the ‘monomer’ and ‘excimer’ phosphorescence of (tbtpy)Pt(L) units, respectively. The ‘excimer’ component is due to intermolecular interactions between these units in the solid state. This feature seems to be especially pronounced in complex  $1$ , which may be affected by additional weak Pt(II)⋯Pt(II) interactions (absent in solid **L-Pt**, see results above).

The PL properties of the heterotrinnuclear solid complex  $1$ , such as the emission spectral shape, intensity and lifetime, significantly depend on the temperature. However, all these parameters do not show any specific correlation with the temperature-dependent magnetization – measured on the sample from the same preparation (e.g., cf. Fig. 3 and 7c). Taking also into account the very similar PL properties of  $1$  and **L-Pt**, we conclude that the PL of  $1$  (‘localized’ on the ligand units) is practically not affected by the spin transition core.

The steady-state absorption and emission spectra of  $1$  and **L-Pt** were recorded in a dichloromethane ( $\text{CH}_2\text{Cl}_2$ ) solution (Fig. 8). The photophysical data are summarized in Table 3.

A comparison of  $1$  and **L-Pt** demonstrates that the absorption and emission of  $1$  are dominated by **L-Pt** ligands. The presence of two such units doubles the extinction of  $1$  as compared with **L-Pt** in the absorption range of  $\sim 290$ – $450\text{ nm}$ . Apparently, the  $\text{Fe}^{II}$ -bpp unit in  $1$  contributes a relatively weak, long-wavelength absorption band at  $\sim 480\text{ nm}$  (Fig. 8a), which does not contribute to the emission/excitation spectrum (Fig. 8b).

### 2.5. Femtosecond-transient absorption spectroscopy

Additional insights into the photophysics of  $1$  are obtained by means of ultrafast transient absorption spectroscopy. Excitation of  $1$  in  $\text{CH}_2\text{Cl}_2$  at  $350\text{ nm}$  yields difference spectra that become stationary on a time scale of a few ps (Fig. 9a).

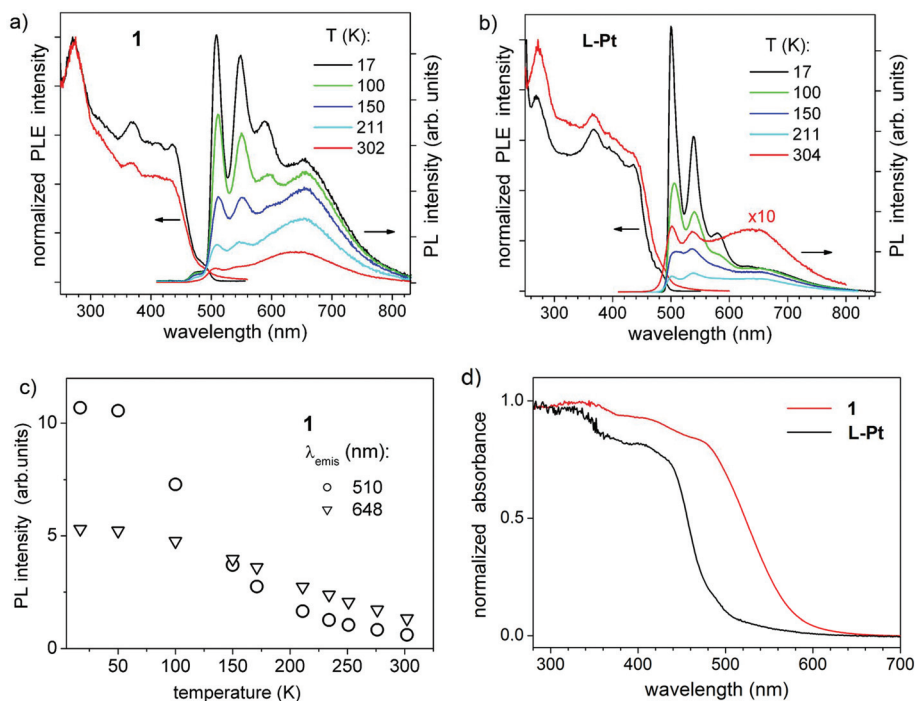


**Fig. 7** (a, b) Photoluminescence excitation (PLE) and emission spectra of solid **1** and L-Pt at low (20 K) and ambient temperature. The PLE spectra were recorded at 580 nm ( $T = 17$  K) and 660 nm (ambient temperature) and emission spectra were excited at 370 nm. (c) Intensities of the PL peaks of **1** at 510 and 648 nm as a function of temperature. (d) Absorption spectra of solid **1** and L-Pt at ambient temperature.

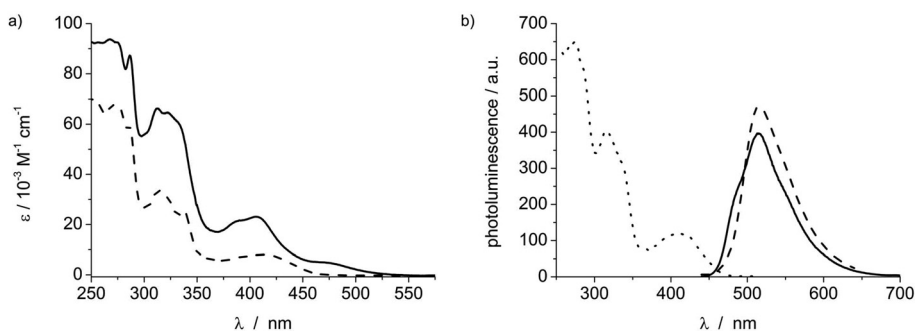


**Fig. 8** (a) Absorption and (b) emission spectra of **1** and L-Pt (solid and dashed lines, respectively,  $\lambda_{\text{exc}}(\mathbf{1}) = 323$  nm,  $\lambda_{\text{exc}}(\text{L-Pt}) = 337$  nm) in a  $\text{CH}_2\text{Cl}_2$  solution; panel (b) shows the emission/excitation spectrum of **1** (dotted line, recorded at  $\lambda_{\text{emis}} = 530$  nm).

**Table 3** Summarized photophysical data for **1** and L-Pt in  $\text{CH}_2\text{Cl}_2$  at ambient temperature

Complex	Absorption, $\lambda(\text{max})$ [nm] ( $\epsilon/1000 \text{ dm}^3 \text{ mol}^{-1} \text{ cm}^{-1}$ )	Emission, $\lambda(\text{max})$ [nm]
<b>1</b>	490 (3), 477 (5), 406 (23), 385 (21), 333 (60), 322 (65), 312 (66), 286 (87)	515
<b>L-Pt</b>	410 (8), 337 (25), 321 (31), 313 (34), 286 (60), 270 (68), 249 (70)	516

The decay associated spectra  $A_1$  and  $A_2$  of a biexponential global fit with  $\tau_1 = 0.3$  and  $\tau_2 = 5.2$  ps are given in Fig. 9b (*cf.* the Experimental section). Among fast relaxation processes deactivating the Franck-Condon state the most interesting

feature in the transient difference spectra is the fast (within 5.2 ps or less) formation of the negative bleach signal around 470 nm, which persists for longer than 1 ns (the time scale of our experiment), together with positive absorption changes at smaller and larger wavelengths. Note that the bleach band at 470 nm matches very well, in peak position as well as in spectral width, the static absorption band of the  $\text{Fe}^{\text{II}}$ -bpp moiety, whereas the excitation at 350 nm dominantly excites the  $\text{Pt}^{\text{II}}$ -terpy units (*cf.* above, the text and Fig. 8a). Since, *vice versa*, the latter do not show significant absorption around 470 nm, the bleach at 470 nm can only be explained by energy transfer from the initially excited  $\text{Pt}^{\text{II}}$ -terpy units to the  $\text{Fe}^{\text{II}}$ -bpp unit. Thus the late difference spectra at 35 and 200 ps (Fig. 9a) and  $A_0$  (Fig. 9b), displaying basically the same stationary states on

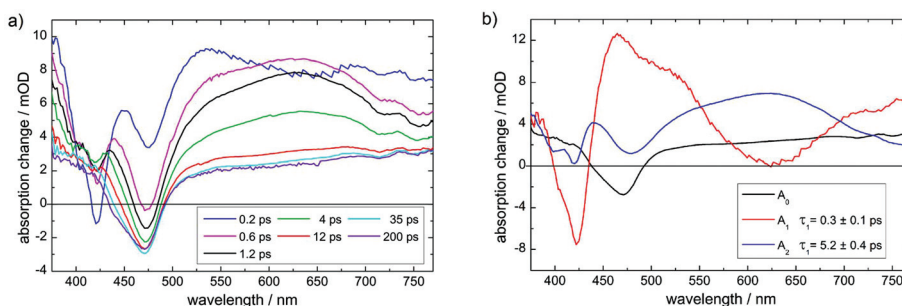


**Fig. 9** (a) Transient difference spectra of **1** in  $\text{CH}_2\text{Cl}_2$  at ambient temperature after photoexcitation at 350 nm at various pump–probe delay times. (b) Results of global analysis by a biexponential fit (cf. Experimental section).

this timescale, can be assigned to the absorption difference between the depleted  $\text{Pt}^{\text{II}}$ -terpy units and the  $\text{Fe}^{\text{II}}$ -bpp unit (negative band) in their electronic ground state on the one hand and excited states formed by photoexcitation on the other hand. Both features have a lifetime longer than 1 ns. Since the proposed energy transfer to the  $\text{Fe}^{\text{II}}$ -bpp unit is quite fast, this process may significantly contribute to the quenching of the excited  $\text{Pt}^{\text{II}}$ -terpy units and thus to the quenching of the (moderately intense) PL of **1**. Taking into account a similarity between the PL/absorption properties of **1** in the solid state and in solution (see above), a similarly efficient PL quenching by energy transfer to the  $\text{Fe}^{\text{II}}$ -bpp unit likely also occurs in the solid state. Ideally, the energy transfer rate and, correspondingly, the PL intensity might be modulated by the spin state of  $\text{Fe}^{\text{II}}$  as a function of temperature. However, the PL data as discussed above show that this effect – if present in the solid state for  $1^{\text{L}}$  species – is small and practically ‘hidden’ as compared to the general temperature dependence of the PL (similar to that of the solid ligand compound **L-Pt**). Whether or not the participating electronic states of the  $\text{Fe}^{\text{II}}$ -bpp unit can be related to  $1^{\text{L}}$ ,  $1^{\text{H}}$  or  $1^{\text{H}}$  observed in the LIESST experiment in solid **1** (see above) is up to further investigation and the subject of our studies on photoinduced spin state switching.<sup>91</sup>

### 3. Experimental section

#### 3.1. Materials, methods and instrumentation

**General.** All reagents and solvents used in this study are commercially available and were used without any further purification, except where stated. 2,6-Di(pyrazol-1-yl)-4-(trimethylsilylethynyl)pyridine was synthesized according to a reported procedure.<sup>48</sup>  $^1\text{H}$  and  $^{13}\text{C}$  NMR spectroscopic data were recorded on a Bruker Ultrashield Plus 500 spectrometer with solvent-protons as an internal standard. Mass spectrometric data were acquired with a Bruker MicroTOF-Q II ESI-TOF. Infrared spectra were recorded using KBr-pressed pellets with a Perkin-Elmer Spectrum GX FT-IR spectrometer in the region of 4000–400  $\text{cm}^{-1}$ . Elemental analyses were carried out using a Vario Micro Cube. Electronic absorption spectroscopy was conducted using a Varian Cary 50 Scan UV-vis spectrophotometer.

#### 3.2. Magnetic susceptibility

All herein reported susceptibility measurements were performed using a SQUID magnetometer (Quantum Design, model MPMS-XL-5). In all cases, the temperature dependence of the magnetic moment was recorded at  $B = 0.1$  T as an external magnetic field. The temperature sweeping rate was 1  $\text{K min}^{-1}$  and was the same for cooling and heating modes. Gelatine capsules as sample containers were used for the measurement in the temperature range 5–370 K. The very small diamagnetic contribution of the gelatine capsule had a negligible contribution to the overall magnetisation, which was dominated by the sample. The diamagnetic corrections of the molar magnetic susceptibilities were applied using Pascal’s constants.<sup>92</sup> All magnetic data were corrected for this background value and then processed into the  $\chi T$  product function.

#### 3.3. Single crystal X-ray diffraction

Single crystal X-ray diffraction data were collected using a STOE IPDS 2 ( $1^{\text{H}}$ ) or STOE IPDS 2T ( $1^{\text{L}}$  and **L-Pt**) diffractometer with graphite monochromated Mo- $K\alpha$  radiation (0.71073 Å). Using Olex2,<sup>93</sup> the structure was solved with the ShelXS<sup>94</sup> structure solution program using direct methods and refined with the ShelXL<sup>94</sup> refinement package using Least Squares minimisation. Refinement was performed with anisotropic displacement factors for all non-hydrogen atoms (disordered atoms were refined isotropically). Hydrogen atoms were modelled on idealized positions. Crystal data and structure refinement information for crystals of  $1^{\text{H}}$ ,  $1^{\text{L}}$ , and **L-Pt** are available in Table S1 of the ESI.†

#### 3.4. Photoluminescence study

Photoluminescence (PL) measurements were performed using a Spex Fluorolog-3 spectrometer equipped with a 450 W xenon light source, double excitation and emission monochromators and a thermoelectrically cooled Hamamatsu R9910 photo-multiplier as a detector. Solid samples (polycrystalline powders) were dispersed in viscous polyfluoroester (ABCR GmbH), layered between two 1 mm thick quartz plates and mounted on the cold finger of an optical closed-cycle cryostat (Leybold) operating at  $\sim 15$ –350 K. Emission was collected at  $\sim 30^\circ$  angle

relative to the excitation light beam. All emission spectra are presented corrected for the wavelength-dependent response of the spectrometer and the detector (in relative photon flux units). Solution phase PL measurements were performed using a Varian Cary Eclipse Fluorescence Spectrophotometer at ambient temperature.

### 3.5. Synthesis of 1

[(tbtpy)Pt(L)](BF<sub>4</sub>) (0.1 g, 0.109 mmol) was dissolved in freshly distilled CH<sub>3</sub>CN (20 mL). The solution was degassed with argon. Fe(H<sub>2</sub>O)<sub>6</sub>(BF<sub>4</sub>)<sub>2</sub> (18.39 mg, 0.054 mmol) was added to this yellow solution. The colour changed to orange. The solution was stirred under argon at 50 °C for the time of 14 h. The reaction was stopped and filtered. The filtrate was reduced to dryness.

Elemental analysis: calc. (found) for 1·CH<sub>3</sub>CN·2H<sub>2</sub>O (C<sub>82</sub>H<sub>93</sub>B<sub>4</sub>F<sub>16</sub>FeN<sub>17</sub>O<sub>2</sub>Pt<sub>2</sub>) C, 45.98 (45.90); H, 4.38 (4.20); N, 11.12 (11.01). <sup>1</sup>H NMR (CD<sub>3</sub>CN, *d* = 1.94 ppm, 500 MHz): δ = 67.56 (s (broad), 4H), 60.41 (s, 4H), 40.23 (s(broad), 4H), 39.70 (s(broad), 4H), 8.82 (s (broad), 4H, tpy), 8.33 (s, 4H), 8.28 (s, 4H), 7.77 (s, 4H), 1.52 (s, 18H), 1.45 (s, 36H) ppm. FT-IR (KBr): ν = 3438, 3130, 2964, 2876, 2119, 1618, 1558, 1524, 1507, 1457, 1404, 1372, 1338, 1265, 1204, 1175, 1084, 1055, 918, 896, 863, 766, 632, 610, 521, 419 cm<sup>-1</sup>. MS (ES) in CH<sub>3</sub>CN: *m/z* = 945.3012 [(C<sub>80</sub>H<sub>86</sub>B<sub>2</sub>F<sub>8</sub>FeN<sub>16</sub>Pt<sub>2</sub>)<sup>2+</sup>, [M - 2BF<sub>4</sub>]<sup>+</sup>, 5%), the difference of the measured and the calculated spectrum is smaller than 5 mDa; crystals suitable for X-ray diffraction were grown by slow evaporation of solutions in CH<sub>2</sub>Cl<sub>2</sub>. For the magnetic measurement the polycrystalline sample was collected from test tubes by removing the dichloromethane mother liquor and leaving the sample under a weak stream of argon before the measurement. An <sup>57</sup>Fe-enriched sample of 1 was prepared as described above using <sup>57</sup>Fe(H<sub>2</sub>O)<sub>6</sub>(BF<sub>4</sub>)<sub>2</sub>, which was described elsewhere employing AgBF<sub>4</sub> instead of Ag(SO<sub>3</sub>CF<sub>3</sub>).<sup>83</sup>

### 3.6 Synthesis of L-Pt

[(tbtpy)PtCl](BF<sub>4</sub>) (0.25 g, 0.347 mmol, 1 eq.) was dissolved in CH<sub>2</sub>Cl<sub>2</sub> (15 mL) and then NEt<sub>3</sub> (7 mL) was added. In a second flask 2,6-di(pyrazol-1-yl)-4-(trimethylsilylethynyl)pyridine (0.136 g, 0.44 mmol, 1.1 eq.) was dissolved in THF (20 mL), MeOH (10 mL), and H<sub>2</sub>O (2 mL). The solutions were stirred and degassed with argon for 15 minutes. The dichloromethane solution was transferred to the latter one using a double cannula before K<sub>2</sub>CO<sub>3</sub> (0.61 g, 4 mmol, 10 eq.) was added. Finally, CuI (8.36 mg, 0.04 mmol, 0.1 eq.) was added to the reaction. 25 mL of degassed dichloromethane was added after some precipitate formed. The reaction was stirred overnight at room temperature and then stopped. Solvents were removed at reduced pressure and the residue was dissolved in CH<sub>2</sub>Cl<sub>2</sub> and water. The organic phase was separated of the inorganic and the latter was washed twice with 20 mL CH<sub>2</sub>Cl<sub>2</sub>. The combined organic phases were dried over Na<sub>2</sub>SO<sub>4</sub>, filtered and reduced to dryness. The crude product was purified by column chromatography on SiO<sub>2</sub> starting with EtOAc to remove organic species, switching later to CH<sub>2</sub>Cl<sub>2</sub> with 3% CH<sub>3</sub>OH. The yellow main

fraction was collected and dried overnight *in vacuo*. Yield: 0.224 g (70%).

<sup>1</sup>H NMR (CD<sub>3</sub>CN, 500 MHz): δ = 8.99 (d, 2H, <sup>3</sup>*J* = 6.0 Hz, tpy6), 8.46 (d, 2H, <sup>4</sup>*J* = 0.4 Hz, <sup>3</sup>*J* = 2.1 Hz, bpp5), 8.20 (s, 2H, tpy3'), 8.15 (d, 2H, <sup>4</sup>*J* = 2.0 Hz, tpy3), 7.73 (s, 2H, bpp3'), 7.69 (dd, 2H, <sup>4</sup>*J* = 2.1 Hz, <sup>3</sup>*J* = 6.0 Hz, tpy5), 7.65 (d, 2H, <sup>4</sup>*J* = 0.5 Hz, <sup>3</sup>*J* = 1.5 Hz, bpp3), 6.48 (d, 2H, *J* = 1.6 Hz, *J* = 2.6 Hz, bpp4), 1.53 (s, 9H, tpy), 1.46 (s, 18H, tpy) ppm. <sup>13</sup>C NMR (CDCl<sub>3</sub>, 300 MHz): δ = 170.23, 167.25, 166.51, 157.94, 153.46, 149.49, 141.93, 139.86, 126.73, 125.44, 122.66, 120.81, 111.26, 108.24, 107.71, 100.88, 59.56, 36.67, 35.71, 29.26, 28.95, ppm. MS (ES): *m/z* = 830.41 [(C<sub>40</sub>H<sub>43</sub>N<sub>8</sub>Pt)<sup>+</sup>, [M - BF<sub>4</sub>]<sup>+</sup>, 100%), UV-vis [λ/[nm] (ε/[1000 dm<sup>3</sup> mol<sup>-1</sup> cm<sup>-1</sup>)] (in CH<sub>2</sub>Cl<sub>2</sub>, *c* = 3.02 μmol L<sup>-1</sup>): λ(ε) = 410 (8), 337 (25), 321 (31), 313 (34), 286 (60), 270 (68), 249 (70); FT-IR (KBr): ν = 3436, 2918, 2875, 2119, 1608, 1545, 1523, 1462, 1426, 1399, 1372, 1257, 1205, 1174, 1123, 1106, 1083, 1042, 954, 918, 889, 842, 790, 772, 628, 608, 558, 419 cm<sup>-1</sup>.

### 3.7 Mössbauer experiments

The field- and temperature dependent Mössbauer spectra were measured with a closed-cycle cryostat with a superconducting magnet, which is described elsewhere.<sup>95</sup> Magnetically split spectra were simulated on the basis of the Hamiltonian approximation.<sup>84–87,96,97</sup> The LIESST experiment was carried out with a specially designed sample rod, which allows one to illuminate the sample almost homogeneously at *T* = 4.2 K with laser light *via* a fibre optic feedthrough. The input power of the used red diode laser (λ = 635 nm) was *P*<sub>in</sub> = 81 mW.

### 3.8 Nuclear resonance vibrational spectroscopy (NRVS) experiments

NIS experiments were performed at the Dynamics Beamline P01, Petra III, DESY in Hamburg, Germany, under application No. 0345. The powder sample was measured in a helium closed cycle cryostat at 80 and 300 K. The NIS data were collected during several scans within the energy range -10 to 80 meV with 0.25 meV step size and 6 s measuring time. The experimental energy resolution of the set-up was ~1 meV (~8 cm<sup>-1</sup>). The experimentally determined partial density of vibrational states (pDOS) was generated with a binning of 0.5 meV.

### 3.9 Density functional theory calculations

Electronic energies have been calculated for the optimized geometries of the molecular structures of 1<sup>L</sup> and 1<sup>H</sup> (Fig. 2). All calculations were performed with the GAUSSIAN09 program system.<sup>98</sup> The functional B3LYP<sup>99</sup> (Becke's exchange functional) and the split valence basis set CEP-31G were used for optimisations, electronic energy, and frequency calculations. In all cases the ultrafine grid option was used for integration. The first optimisations for LS (multiplicity *M* = 1) and HS (multiplicity *M* = 5) complexes were performed for the +4 cation of the complexes. This led to a HS isomer of C<sub>2</sub> symmetry, with a Pt-Fe-Pt angle of 180°. The second model includes additionally four tetrafluoroborate anions. In this case the starting geo-

metry ( $L = 0$ ,  $M = 5$ ) was based on the molecular structure  $\mathbf{1}^H$ , including the four charge-balancing anions. The thus optimised HS structure revealed a bend structure with a Pt–Fe–Pt angle of  $150^\circ$  which is in reasonable accordance with the Pt–Fe–Pt angle of  $160^\circ$  as determined by the X-ray diffraction experiments.

Complex	$\mathbf{1}^L$ (X-ray)	LS-symm (DFT)	$\mathbf{1}^H$ (X-ray)	HS-4BF <sub>4</sub> (DFT)	HS-symm (DFT)
Spin state	LS	LS	HS	HS	HS
Symmetry	$C_2$	$C_2$	$C_1$	$C_1$	$C_1$
Symmetry of Fe(II) environment	$C_2$	$D_{2d}$	$C_1$	$C_1$	$C_2$
	(max $D_2$ )			(max. $C_2$ )	(max. $D_{2d}$ )
>Pt–Fe–Pt/ $^\circ$	170	180	160	150	180
>N <sub>py</sub> –Fe–N <sub>py</sub> / $^\circ$	179	180	157	162	180
>trans-N <sub>pyz</sub> –Fe–N <sub>pyz</sub>	160.5, 160.5	160, 160	140, 146	146, 149	148, 148

Thus, the DFT modelling confirms two high-spin structures differing in symmetry, the first one revealing a perfectly linear alignment of the Pt–Fe–Pt' atoms (corresponding to  $\mathbf{1}^L$ ), while the second shows a significant bending (corresponding to  $\mathbf{1}^H$ ). For an isolated complex +4 cation, a more symmetric geometry is obtained. A structure close to the HS structure  $\mathbf{1}^H$  is observed when the BF<sub>4</sub><sup>−</sup> ions are incorporated into the model. The reason for this may be the larger number of ten dichloromethane molecules in the structure of  $\mathbf{1}^H$  compared to three dichloromethane molecules in the structure of  $\mathbf{1}^L$ . Taking into account the similar shape of anions and solvent molecules, it is possible that for the LS structure, the anions are effectively further away from the complex cation than is the case in the HS structure. Therefore we can conclude that the LS structure is better modeled using the isolated +4 cation, while the tetrafluoroborate containing model is fitting the HS structure better.

### 3.10 Femtosecond-transient absorption spectroscopy

The measurements were performed at room temperature according to those described in Chevalier *et al.* (2012).<sup>100</sup> In short,  $\mathbf{1}$  was dissolved in CH<sub>2</sub>Cl<sub>2</sub> (35 mM). To avoid or control, respectively, photodegradation steady state UV/Vis transmission spectra of the sample were recorded regularly before and after transient absorption measurements on a Jasco V-670 photospectrometer. The femtosecond setup is based on a Ti:Sapphire chirped pulse amplifier system (CPA 2001, Clark-MXR), generating pulses at 775 nm with an energy of 200 nJ and duration of 150 fs FWHM (full width at half maximum). Excitation pulses at 350 nm were generated *via* frequency doubling of pulses at 700 nm, obtained from a homebuilt two-stage noncollinear optical parametric amplifier (NOPA). Transient absorption difference spectra were obtained by probing the excited sample volume (*ca.* 200 μm diameter) with broad band laser pulses between 380–730 nm, generated by focusing a fraction of the laser output into a 3 mm thick sapphire window. The transmitted probe light was dispersed and detected by a spectrograph (Andor) with a 517 pixel CCD camera (Stresing). The pump pulse was chopped at half the

laser frequency (988 Hz) and the transmitted probe light detected alternately with and without a preceding excitation of the sample, allowing the calculation of pump-induced difference spectra  $\Delta A(\lambda, t)$  as a function of probe wavelength and pump–probe delay. The transient UV/Vis data were analysed by means of a global multiexponential fit using

$$\Delta A(\lambda, t) = A_0(\lambda) + \sum_{i=1}^n A_i(\lambda) \cdot e^{-t/\tau_i}$$

with  $A_i(\lambda)$  being the decay associated amplitude spectra (DAS) and  $\tau_i$  the corresponding time constants.  $A_0(\lambda)$  represents the difference spectrum after “infinite” delay times. Only delay times  $t > 200$  fs were considered for the global fit, thereby omitting the time regime of the system response (150 fs).

## 4. Conclusions

A heterotrinary [Pt<sub>2</sub>Fe] spin crossover complex was successfully developed and synthesized employing a ditopic bridging bpp-alkynyl ligand **L** and alkynyl coordinated Pt<sup>II</sup> terpy units: [Fe<sup>II</sup>(L–Pt<sup>II</sup>)<sub>2</sub>]<sub>2</sub>(BF<sub>4</sub>)<sub>2</sub> (**1**). We identified two different types of crystals of **1** which differ only in the number of co-crystallized solvent molecules,  $\mathbf{1}^H$  (1·3.5CH<sub>2</sub>Cl<sub>2</sub>) and  $\mathbf{1}^L$  (1·10CH<sub>2</sub>Cl<sub>2</sub>); while  $\mathbf{1}^L$  shows a reversible SCO with a transition temperature of 268 K, the analogous compound  $\mathbf{1}^H$  does not show any SCO and remains blocked in the HS state over the full temperature range investigated. The temperature-dependent magnetic properties of  $\mathbf{1}^H$  and  $\mathbf{1}^L$  were complementarily studied by Mössbauer spectroscopy, showing good agreement of the data. It has been shown that  $\mathbf{1}^L$  performs thermal spin crossover and that  $\mathbf{1}^L$  can be excited to a LIESST state by irradiation with red light. The vibrational properties of **1** were investigated by experimental nuclear resonance vibrational spectroscopy. The experimentally determined partial density of vibrational states (pDOS) is in good agreement with the DFT-based simulation of the pDOS. The vibrational modes of the different components were assigned and visualized in movies. The spin marker bands determined from the iron ligand vibrations of **1** as a function of the temperature confirm the magnetic properties. In addition, the photophysical properties of **1** and L–Pt were investigated in the solid state and in solution. The PL (phosphorescence) properties of **1** and L–Pt are similar as the PL originates from the Pt<sup>II</sup> terpy units and significantly depend on the temperature in the solid state. However, no significant influence of the spin state on the PL of **1** was observed. On the other hand, the ultrafast transient absorption spectroscopy of **1** in solution indicated a possibility of an efficient (ps time scale) PL quenching channel *via* energy transfer from photoexcited Pt<sup>II</sup> terpy units to the Fe<sup>II</sup>-moiety. Ideally, this channel and, as a result, the PL intensity might be modulated by the spin state of Fe<sup>II</sup>. However, such a situation is apparently not realized in solid complex **1**. In conclusion, we have presented a rare example of a luminescent SCO complex and demonstrated that even small changes in the solid state structure related to the extended ligand system may

have a strong influence on the spin state switching properties due to unbalanced structural constraints in the Fe<sup>II</sup>-chelating ligand environment.

## Acknowledgements

We acknowledge support from the Deutsche Forschungsgemeinschaft (DFG) through TRR 88 "3MET" (A1, A4, C4, C5, and C6).

## Notes and references

- 1 E. C. Constable, *Coord. Chem. Rev.*, 2008, **252**, 842–855.
- 2 H. Hofmeier and U. S. Schubert, *Chem. Soc. Rev.*, 2004, **33**, 373.
- 3 U. Schubert, H. Hofmeier and G. R. Newkome, *Modern terpyridine chemistry*, Wiley-VCH, Weinheim, 2006.
- 4 A. Wild, A. Winter, F. Schlütter and U. S. Schubert, *Chem. Soc. Rev.*, 2011, **40**, 1459–1511.
- 5 E. C. Constable, *Chem. Soc. Rev.*, 2007, **36**, 246–253.
- 6 T. K. Ronson, T. Lazarides, H. Adams, S. J. A. Pope, D. Sykes, S. Faulkner, S. J. Coles, M. B. Hursthouse, W. Clegg, R. W. Harrington and M. D. Ward, *Chem. – Eur. J.*, 2006, **12**, 9299–9313.
- 7 M. D. Ward, *Coord. Chem. Rev.*, 2007, **251**, 1663–1677.
- 8 M. G. Pfeffer, B. Schäfer, G. Smolentsev, J. Uhlig, E. Nazarenko, J. Guthmüller, C. Kuhnt, M. Wächter, B. Dietzek, V. Sundström and S. Rau, *Angew. Chem., Int. Ed.*, 2015, **54**, 5044–5048.
- 9 H. Ozawa and K. Sakai, *Chem. Commun.*, 2011, **47**, 2227.
- 10 A. M. W. Cargill Thompson, *Coord. Chem. Rev.*, 1997, **160**, 1–52.
- 11 R.-A. Fallahpour, *Synthesis*, 2003, 0155–0184.
- 12 M. Heller and U. S. Schubert, *Eur. J. Org. Chem.*, 2003, 947–961.
- 13 M. A. Halcrow, *Coord. Chem. Rev.*, 2005, **249**, 2880–2908.
- 14 M. A. Halcrow, *Coord. Chem. Rev.*, 2009, **253**, 2493–2514.
- 15 M. A. Halcrow, *New J. Chem.*, 2014, **38**, 1868–1882.
- 16 M. J. Remuinan, H. Roman, M. T. Alonso and J. C. Rodríguez-Ubis, *J. Chem. Soc., Perkin Trans. 2*, 1993, 1099.
- 17 J. C. Rodríguez-Ubis, R. Sedano, G. Barroso, O. Juanes and E. Brunet, *Helv. Chim. Acta*, 1997, **80**, 86–96.
- 18 M. Mato-Iglesias, T. Rodríguez-Blas, C. Platas-Iglesias, M. Starck, P. Kadjane, R. Ziessel and L. Charbonnière, *Inorg. Chem.*, 2009, **48**, 1507–1518.
- 19 P. Kadjane, M. Starck, F. Camerel, D. Hill, N. Hildebrandt, R. Ziessel and L. J. Charbonnière, *Inorg. Chem.*, 2009, **48**, 4601–4603.
- 20 K. Senthil Kumar, B. Schäfer, S. Lebedkin, L. Karmazin, M. M. Kappes and M. Ruben, *Dalton Trans.*, 2015, **44**, 15611–15619.
- 21 J. Olguín and S. Brooker, *Coord. Chem. Rev.*, 2011, **255**, 203–240.
- 22 *Spin Crossover in Transition Metal Compounds I-III: Top.* *Curr. Chem.*, ed. P. Gülich and H. A. Goodwin, Springer, Berlin, Heidelberg, 2004, vol. 233–235.
- 23 I. Šalitroš, N. T. Madhu, R. Boča, J. Pavlik and M. Ruben, *Monatsh. Chem.*, 2009, **140**, 695–733.
- 24 P. Gülich, A. Hauser and H. Spiering, *Angew. Chem., Int. Ed.*, 1994, **33**, 2024–2054.
- 25 G. Félix, K. Abdul-Kader, T. Mahfoud, I. A. Gural'skiy, W. Nicolazzi, L. Salmon, G. Molnár and A. Bousseksou, *J. Am. Chem. Soc.*, 2011, **133**, 15342–15345.
- 26 A. Rotaru, I. A. Gural'skiy, G. Molnár, L. Salmon, P. Demont and A. Bousseksou, *Chem. Commun.*, 2012, **48**, 4163.
- 27 S. Bonhommeau, T. Guillon, L. M. Lawson Daku, P. Demont, J. Sanchez Costa, J.-F. Létard, G. Molnár and A. Bousseksou, *Angew. Chem., Int. Ed.*, 2006, **45**, 1625–1629.
- 28 J. A. Real, I. Castro, A. Bousseksou, M. Verdager, R. Burriel, M. Castro, J. Linares and F. Varret, *Inorg. Chem.*, 1997, **36**, 455–464.
- 29 M. Bernien, D. Wiedemann, C. F. Hermanns, A. Krüger, D. Rolf, W. Kroener, P. Müller, A. Grohmann and W. Kuch, *J. Phys. Chem. Lett.*, 2012, **3**, 3431–3434.
- 30 T. Miyamachi, M. Gruber, V. Davesne, M. Bowen, S. Boukari, L. Joly, F. Scheurer, G. Rogez, T. K. Yamada, P. Ohresser, E. Beaurepaire and W. Wulfhekel, *Nat. Commun.*, 2012, **3**, 938.
- 31 T. G. Gopakumar, F. Matino, H. Naggert, A. Bannwarth, F. Tuczek and R. Berndt, *Angew. Chem., Int. Ed.*, 2012, **51**, 6262–6266.
- 32 V. A. Money, J. Elhaik, M. A. Halcrow and J. A. K. Howard, *Dalton Trans.*, 2004, 1516.
- 33 C. Carbonera, J. Sanchez Costa, V. A. Money, J. Elhaik, J. A. K. Howard, M. A. Halcrow and J.-F. Letard, *Dalton Trans.*, 2006, 3058.
- 34 I. Šalitroš, O. Fuhr, A. Eichhöfer, R. Kruk, J. Pavlik, L. Dlhán, R. Boča and M. Ruben, *Dalton Trans.*, 2012, **41**, 5163.
- 35 T. Vermonden, D. Branowska, A. T. Marcelis and E. J. Sudhölter, *Tetrahedron*, 2003, **59**, 5039–5045.
- 36 J. Elhaik, C. M. Pask, C. A. Kilner and M. A. Halcrow, *Tetrahedron*, 2007, **63**, 291–298.
- 37 L. J. Kershaw Cook, H. J. Shepherd, T. P. Comyn, C. Baldé, O. Cespedes, G. Chastanet and M. A. Halcrow, *Chem. – Eur. J.*, 2015, **21**, 4805–4816.
- 38 L. J. Kershaw Cook, R. Kulmaczewski, S. A. Barrett and M. A. Halcrow, *Inorg. Chem. Front.*, 2015, **2**, 662–670.
- 39 L. J. Kershaw Cook, F. L. Thorp-Greenwood, T. P. Comyn, O. Cespedes, G. Chastanet and M. A. Halcrow, *Inorg. Chem.*, 2015, **54**, 6319–6330.
- 40 A. Abhervé, M. Clemente-León, E. Coronado, C. J. Gómez-García and M. López-Jordà, *Dalton Trans.*, 2014, **43**, 9406.
- 41 M. Nihei, L. Han and H. Oshio, *J. Am. Chem. Soc.*, 2007, **129**, 5312–5313.
- 42 M. Nihei, N. Takahashi, H. Nishikawa and H. Oshio, *Dalton Trans.*, 2011, **40**, 2154–2156.

- 43 Y. Hasegawa, K. Takahashi, S. Kume and H. Nishihara, *Chem. Commun.*, 2011, **47**, 6846.
- 44 K. Takahashi, Y. Hasegawa, R. Sakamoto, M. Nishikawa, S. Kume, E. Nishibori and H. Nishihara, *Inorg. Chem.*, 2012, **51**, 5188–5198.
- 45 Y. Hasegawa, R. Sakamoto, K. Takahashi and H. Nishihara, *Inorg. Chem.*, 2013, **52**, 1658–1665.
- 46 C. Rajadurai, O. Fuhr, R. Kruk, M. Ghafari, H. Hahn and M. Ruben, *Chem. Commun.*, 2007, 2636.
- 47 C. Rajadurai, Z. Qu, O. Fuhr, B. Gopalan, R. Kruk, M. Ghafari and M. Ruben, *Dalton Trans.*, 2007, 3531.
- 48 R. Chandrasekar, F. Schramm, O. Fuhr and M. Ruben, *Eur. J. Inorg. Chem.*, 2008, **2008**, 2649–2653.
- 49 N. T. Madhu, I. Salitros, F. Schramm, S. Klyatskaya, O. Fuhr and M. Ruben, *C. R. Chim.*, 2008, **11**, 1166–1174.
- 50 F. Schramm, R. Chandrasekar, T. A. Zevaco, M. Rudolph, H. Görls, W. Poppitz and M. Ruben, *Eur. J. Inorg. Chem.*, 2009, **2009**, 53–61.
- 51 I. Šalitroš, J. Pavlik, R. Boča, O. Fuhr, C. Rajadurai and M. Ruben, *CrystEngComm*, 2010, **12**, 2361.
- 52 M. Cavallini, I. Bergenti, S. Milita, J. C. Kengne, D. Gentili, G. Ruani, I. Salitros, V. Meded and M. Ruben, *Langmuir*, 2011, **27**, 4076–4081.
- 53 V. Meded, A. Bagrets, K. Fink, R. Chandrasekar, M. Ruben, F. Evers, A. Bernand-Mantel, J. S. Seldenthuis, A. Beukman and H. S. J. van der Zant, *Phys. Rev. B: Condens. Matter*, 2011, **83**, 245415.
- 54 R. González-Prieto, B. Fleury, F. Schramm, G. Zoppellaro, R. Chandrasekar, O. Fuhr, S. Lebedkin, M. Kappes and M. Ruben, *Dalton Trans.*, 2011, **40**, 7564.
- 55 I. Šalitroš, O. Fuhr, R. Kruk, J. Pavlik, L. Pogány, B. Schäfer, M. Tatarko, R. Boča, W. Linert and M. Ruben, *Eur. J. Inorg. Chem.*, 2013, **2013**, 1049–1057.
- 56 I. Šalitroš, L. Pogány, M. Ruben, R. Boča and W. Linert, *Dalton Trans.*, 2014, **43**, 16584–16587.
- 57 E. J. Devid, P. N. Martinho, M. V. Kamalakar, I. Šalitroš, Ú. Prendergast, J.-F. Dayen, V. Meded, T. Lemma, R. González-Prieto, F. Evers, T. E. Keyes, M. Ruben, B. Doudin and S. J. van der Molen, *ACS Nano*, 2015, **9**, 4496–4507.
- 58 N. Chandrasekhar and R. Chandrasekar, *Chem. Commun.*, 2010, **46**, 2915.
- 59 L. J. Kershaw Cook, J. Fisher, L. P. Harding and M. A. Halcrow, *Dalton Trans.*, 2015, **44**, 9417–9425.
- 60 S. Basak, P. Hui, S. Boodida and R. Chandrasekar, *J. Org. Chem.*, 2012, **77**, 3620–3626.
- 61 A. K. Botcha, S. Basak and R. Chandrasekar, *RSC Adv.*, 2014, **4**, 34760.
- 62 C. A. Tovee, C. A. Kilner, S. A. Barrett, J. A. Thomas and M. A. Halcrow, *Eur. J. Inorg. Chem.*, 2010, **2010**, 1007–1012.
- 63 C.-W. Chan, L.-K. Cheng and C.-M. Che, *Coord. Chem. Rev.*, 1994, **132**, 87–97.
- 64 M. Hissler, J. E. McGarrah, W. B. Connick, D. K. Geiger, S. D. Cummings and R. Eisenberg, *Coord. Chem. Rev.*, 2000, **208**, 115–137.
- 65 C. E. Whittle, J. A. Weinstein, M. W. George and K. S. Schanze, *Inorg. Chem.*, 2001, **40**, 4053–4062.
- 66 V. W.-W. Yam, R. P.-L. Tang, K. M.-C. Wong and K.-K. Cheung, *Organometallics*, 2001, **20**, 4476–4482.
- 67 Q.-Z. Yang, L.-Z. Wu, Z.-X. Wu, L.-P. Zhang and C.-H. Tung, *Inorg. Chem.*, 2002, **41**, 5653–5655.
- 68 F. N. Castellano, I. E. Pomestchenko, E. Shikhova, F. Hua, M. L. Muro and N. Rajapakse, *Coord. Chem. Rev.*, 2006, **250**, 1819–1828.
- 69 M. L. Muro, S. Diring, X. Wang, R. Ziessel and F. N. Castellano, *Inorg. Chem.*, 2008, **47**, 6796–6803.
- 70 R. Ziessel, S. Diring and P. Retailleau, *Dalton Trans.*, 2006, 3285.
- 71 J. A. Real, E. Andres, M. C. Munoz, M. Julve, T. Granier, A. Bousseksou and F. Varret, *Science*, 1995, **268**, 265–267.
- 72 N. Moliner, C. Muñoz, S. Létard, X. Solans, N. Menéndez, A. Goujon, F. Varret and J. A. Real, *Inorg. Chem.*, 2000, **39**, 5390–5393.
- 73 X. Bao, H. J. Shepherd, L. Salmon, G. Molnár, M.-L. Tong and A. Bousseksou, *Angew. Chem., Int. Ed.*, 2013, **52**, 1198–1202.
- 74 O. Iasco, E. Rivière, R. Guillot, M. Buron-Le Cointe, J.-F. Meunier, A. Bousseksou and M.-L. Boillot, *Inorg. Chem.*, 2015, **54**, 1791–1799.
- 75 C. Lochenie, K. G. Wagner, M. Karg and B. Weber, *J. Mater. Chem. C*, 2015, **3**, 7925–7935.
- 76 V. W.-W. Yam, K. M.-C. Wong and N. Zhu, *Angew. Chem., Int. Ed.*, 2003, **42**, 1400–1403.
- 77 P. Xu, H. Wu, H. Jia, S. Ye and P. Du, *Organometallics*, 2014, **33**, 2738–2746.
- 78 C. Rajadurai and M. Ruben, *EU Pat.*, 2053049A120090429, 2009.
- 79 (a) K. Sonogashira, T. Yatake, Y. Tohda, S. Takahashi and N. Hagihara, *J. Chem. Soc., Chem. Commun.*, 1977, 291; (b) K. Sonogashira, S. Takahashi and N. Hagihara, *Macromolecules*, 1977, **10**, 879–880; (c) K. Sonogashira, Y. Fujikura, T. Yatake, N. Toyoshima, S. Takahashi and N. Hagihara, *J. Organomet. Chem.*, 1978, **145**, 101–108.
- 80 B. Schäfer, C. Rajnák, I. Šalitroš, O. Fuhr, D. Klar, C. Schmitz-Antoniak, E. Weschke, H. Wende and M. Ruben, *Chem. Commun.*, 2013, **49**, 10986.
- 81 D. Gentili, N. Demitri, B. Schäfer, F. Liscio, I. Bergenti, G. Ruani, M. Ruben and M. Cavallini, *J. Mater. Chem. C*, 2015, **3**, 7836–7844.
- 82 J. A. Bailey, M. G. Hill, R. E. Marsh, V. M. Miskowski, W. P. Schaefer and H. B. Gray, *Inorg. Chem.*, 1995, **34**, 4591–4599.
- 83 B. Schäfer, J.-F. Greisch, I. Faus, T. Bodenstern, I. Šalitroš, O. Fuhr, K. Fink, V. Schünemann, M. M. Kappes and M. Ruben, *Angew. Chem., Int. Ed.*, 2016, **55**, 10881–10885.
- 84 G. L. Eichhorn and L. G. Marzilli, *Advances in Inorganic Biochemistry*, Elsevier, New York, Amsterdam, Oxford, 1984.
- 85 P. G. Debrunner and A. B. P. Lever and H. B. Gray, *Iron Porphyrins*, VCH, Weinheim, 1989, vol. III, pp. 139–234.

- 86 A. X. Trautwein, E. Bill, E. L. Bominaar and H. Winkler, in *Bioinorganic Chemistry*, Springer, Berlin, Heidelberg, 1991, vol. 78, pp. 1–95.
- 87 V. Schünemann and H. Winkler, *Rep. Prog. Phys.*, 2000, **63**, 263.
- 88 W. Sturhahn, T. S. Toellner, E. E. Alp, X. Zhang, M. Ando, Y. Yoda, S. Kikuta, M. Seto, C. W. Kimball and B. Dabrowski, *Phys. Rev. Lett.*, 1995, **74**, 3832–3835.
- 89 E. Gerdau and H. DeWaaard, *Hyperfine Interact.*, 1999, **123**, DOI: 10.1023/A:1017073002352.
- 90 J. A. Wolny, R. Diller and V. Schünemann, *Eur. J. Inorg. Chem.*, 2012, **2012**, 2635–2648.
- 91 (a) M. M. N. Wolf, R. Groß, C. Schumann, J. A. Wolny, V. Schünemann, A. Dössing, H. Paulsen, J. J. McGarvey and R. Diller, *Phys. Chem. Chem. Phys.*, 2008, **10**, 4264; (b) F. Rupp, K. Chevalier, M. Graf, M. Schmitz, H. Kelm, A. Grün, M. Zimmer, M. Gerhards, C. van Wüllen, H.-J. Krüger and R. Diller, *Chem. – Eur. J.*, 2017, DOI: 10.1002/chem.201604546.
- 92 O. Kahn, *Molecular magnetism*, VCH, New York, NY, 1993.
- 93 O. V. Dolomanov, L. J. Bourhis, R. J. Gildea, J. A. K. Howard and H. Puschmann, *J. Appl. Crystallogr.*, 2009, **42**, 339–341.
- 94 G. M. Sheldrick, *Acta Crystallogr., Sect. A: Fundam. Crystallogr.*, 2008, **64**, 112–122.
- 95 A. Janoschka, G. Svenconis and V. Schünemann, *J. Phys.: Conf. Ser.*, 2010, **217**, 012005.
- 96 T. O. Bauer, M. Schmitz, M. Graf, H. Kelm, H.-J. Krüger and V. Schünemann, *Hyperfine Interact.*, 2014, **226**, 359–363.
- 97 T. O. Bauer, M. Schmitz, M. Graf, H. Kelm, H.-J. Krüger and V. Schünemann, *Hyperfine Interact.*, 2016, **237**, 78.
- 98 M. J. Frisch, G. W. Trucks, H. B. Schlegel, G. E. Scuseria, M. A. Robb, J. R. Cheeseman, G. Scalmani, V. Barone, B. Mennucci, G. A. Petersson, H. Nakatsuji, M. Caricato, X. Li, H. P. Hratchian, A. F. Izmaylov, J. Bloino, G. Zheng, J. L. Sonnenberg, M. Hada, M. Ehara, K. Toyota, R. Fukuda, J. Hasegawa, M. Ishida, T. Nakajima, Y. Honda, O. Kitao, H. Nakai, T. Vreven, J. A. Montgomery Jr., J. E. Peralta, F. Ogliaro, M. J. Bearpark, J. Heyd, E. N. Brothers, K. N. Kudin, V. N. Staroverov, R. Kobayashi, J. Normand, K. Raghavachari, A. P. Rendell, J. C. Burant, S. S. Iyengar, J. Tomasi, M. Cossi, N. Rega, N. J. Millam, M. Klene, J. E. Knox, J. B. Cross, V. Bakken, C. Adamo, J. Jaramillo, R. Gomperts, R. E. Stratmann, O. Yazyev, A. J. Austin, R. Cammi, C. Pomelli, J. W. Ochterski, R. L. Martin, K. Morokuma, V. G. Zakrzewski, G. A. Voth, P. Salvador, J. J. Dannenberg, S. Dapprich, A. D. Daniels, Ö. Farkas, J. B. Foresman, J. V. Ortiz, J. Cioslowski and D. J. Foxg, *Gaussian 09*, Gaussian, Inc., Wallingford, CT, USA, 2009.
- 99 A. D. Becke, *J. Chem. Phys.*, 1993, **98**, 5648.
- 100 K. Chevalier, M. M. N. Wolf, A. Funk, M. Andres, M. Gerhards and R. Diller, *Phys. Chem. Chem. Phys.*, 2012, **14**, 15007.